

See discussions, stats, and author profiles for this publication at: <https://www.researchgate.net/publication/229324769>

Independent Control of Bulk and Interfacial Morphologies of Small Molecular Weight Organic Heterojunction Solar Cells

ARTICLE *in* NANO LETTERS · JULY 2012

Impact Factor: 13.59 · DOI: 10.1021/nl302172w · Source: PubMed

CITATIONS

62

READS

97

7 AUTHORS, INCLUDING:



[Xin Xiao](#)

Yale University

19 PUBLICATIONS 462 CITATIONS

SEE PROFILE



[Siyi Wang](#)

Intel

13 PUBLICATIONS 737 CITATIONS

SEE PROFILE



[Vyacheslav V Diev](#)

Dupont

25 PUBLICATIONS 620 CITATIONS

SEE PROFILE



[Mark Thompson](#)

University of Southern California

312 PUBLICATIONS 34,157 CITATIONS

SEE PROFILE

Independent Control of Bulk and Interfacial Morphologies of Small Molecular Weight Organic Heterojunction Solar Cells

Jeremy D. Zimmerman,[†] Xin Xiao,[†] Christopher Kyle Renshaw,[‡] Siyi Wang,[§] Vyacheslav V. Diev,[§] Mark E. Thompson,[§] and Stephen R. Forrest^{*,†,‡,||}

[†]Department of Electrical Engineering and Computer Science, University of Michigan, Ann Arbor, Michigan 48109, United States

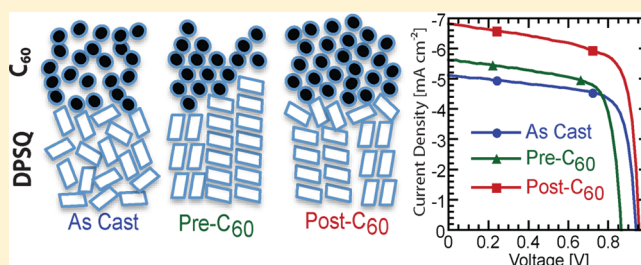
[‡]Department of Physics, University of Michigan, Ann Arbor, Michigan 48109, United States

[§]Department of Chemistry, University of Southern California, Los Angeles, California 90089, United States

^{||}Materials Science and Engineering, University of Michigan, Ann Arbor, Michigan 48109, United States

ABSTRACT: We demonstrate that solvent vapor annealing of small molecular weight organic heterojunctions can be used to independently control the interface and bulk thin-film morphologies, thereby modifying charge transport and exciton dissociation in these structures. As an example, we anneal diphenyl-functionalized squaraine (DPSQ)/C₆₀ heterojunctions before or after the deposition of C₆₀. Solvent vapor annealing of DPSQ before C₆₀ deposition results in molecular order at the heterointerface. Organic photovoltaics based on this process have reduced open circuit voltages and power conversion efficiencies relative to as-cast devices. In contrast, annealing following C₆₀ deposition locks in interface disorder found in unannealed junctions while improving order in the thin-film bulk. This results in an increase in short circuit current by >30% while maintaining the open circuit voltage of the as-cast heterojunction device. These results are analyzed in terms of recombination dynamics at excitonic heterojunctions and demonstrate that the optimal organic photovoltaic morphology is characterized by interfacial disorder to minimize polaron-pair recombination, while improved crystallinity in the bulk increases exciton and charge transport efficiency in the active region.

KEYWORDS: Organic photovoltaic, squaraine, fullerene, annealing, small-molecule organic semiconductor, polaron-pair recombination



In a recent theoretical study by Giebink et al.,^{1,2} it was shown that efficient excitonic heterojunction photovoltaic cells require the minimization of the polaron-pair (PP) recombination rate (k_{ppr}) at the donor–acceptor (D–A) interface. It was suggested that this could be accomplished by decreasing the interaction between donor and acceptor molecules by increasing disorder or by introducing steric hindrance between dissimilar molecules across the D–A interface, thereby inhibiting orbital overlap.^{1,2} Furthermore, optimized organic photovoltaic cells (OPVs) require considerable order within the bulk to minimize cell series resistance while improving the exciton diffusion efficiency.³ These seemingly contradictory materials requirements, that is, (i) reduced orbital overlap at the heterointerface and (ii) order within the bulk layer, have been demonstrated previously using complex, multilayer “cascade” OPV structures, where the individual requirements are met by combining several thin layers of different compositions.⁴

In this work, architectural complexity is avoided by the use of solvent vapor annealing (SVA) of bilayer cells comprising the acceptor, C₆₀, and the donor, 2,4-bis[4-(N,N-diphenylamino)-2,6-dihydroxyphenyl] squaraine (DPSQ, see Figure 1a, inset).^{5,6} We find that the SVA of DPSQ prior to deposition of C₆₀ (i.e., “pre-C₆₀” SVA) results in structural templating of

the C₆₀, providing direct evidence of increased order at the heterojunction, in contrast to the disordered interfaces characteristic of unannealed junctions. The ordered DPSQ/C₆₀ interface results in a significant increase in k_{ppr} and hence a decrease in open circuit voltage (V_{OC}) that reduces the corresponding OPV power conversion efficiency from $\eta_p = 3.6\%$ to 3.4% . In contrast, DPSQ/C₆₀ junctions annealed *after* C₆₀ deposition (or “post-C₆₀ SVA”) have an interface morphology similar to that of the as-cast DPSQ devices that leads to decreased intermolecular interactions compared to pre-C₆₀ devices, but with an improved crystallinity in the bulk layers (and hence improved exciton³ and charge transport^{7,8}) compared to as-cast devices. Hence, the post-C₆₀ process leads to the optimized structure proposed by Giebink et al. in a single bilayer.^{1,2} This results in a reduced PP recombination relative to pre-C₆₀ devices, with a concomitant increase in V_{OC} and short circuit current density, J_{SC} . Relative to as-cast devices, post-C₆₀ OPVs show a substantially increased power conversion efficiency from $\eta_p = 3.6\%$ to 4.8% . These results provide striking evidence that the interface morphology affects

Received: June 8, 2012

Revised: July 10, 2012

Published: July 18, 2012

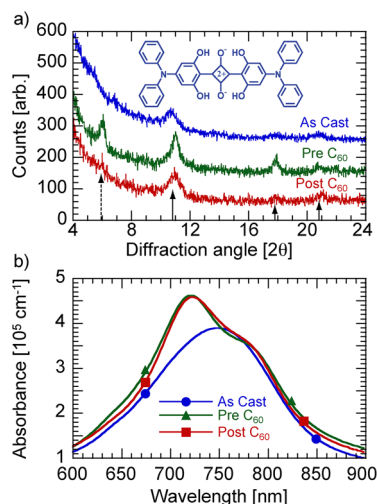


Figure 1. Film morphologies as determined by X-ray diffraction and absorption spectroscopy. (a) X-ray diffraction patterns for as-cast, pre- C_{60} , and post- C_{60} DPSQ/ C_{60} bilayers. The data are offset vertically for clarity. The peak at 5.9° (dashed arrow) is associated with DPSQ, while the peaks at $2\theta = 10.8^\circ$, 17.7° , and 20.7° (solid arrows) are associated with the $\{111\}$, $\{220\}$, and $\{311\}$ planes of C_{60} . Inset: DPSQ molecular structure. (b) Absorption spectra for DPSQ, showing an as-cast sample and aggregation splitting of the absorption peak for pre- C_{60} and post- C_{60} treatments. The C_{60} absorption spectra are not shown and are independent of the annealing process.

the recombination kinetics at organic heterojunctions and that separate control of bulk and interfacial morphologies is required to maximize OPV performance.

We begin by framing our strategy in the context of the model for ideal excitonic heterojunctions of Giebink et al.^{1,2} The process of charge photogeneration is as follows: light absorption in the donor and acceptor layers generates a spatial distribution of excitons⁹ that diffuse to the D–A interface where they dissociate into PPs. The PPs subsequently dissociate into free carriers (polarons) extracted at the contacts.¹ The film morphology^{2,10} (e.g., molecular structure and orientation) and energetics^{1,2,11,12} (including ΔE_{HL} , the energy offset between the highest occupied molecular orbital, HOMO, of the donor, and the lowest unoccupied molecular orbital, LUMO, of the acceptor) of the interface determine V_{OC} and the fill factor (FF). Energy transport within the layers determines J_{SC} and also affects FF. Specifically, V_{OC} in the presence of interfacial traps (assumed, for simplicity, to only exist on the donor side of the heterojunction) is given by:¹

$$qV_{OC} = \Delta E_{HL} - n_D k_B T \ln \left[\left(\frac{k_{PPr}}{k_{PPd}} \right) \frac{k_{rec,n} N_L H_D}{J_X / a_0} \right] \quad (1a)$$

or

$$qV_{OC} = \Delta E_{HL} - n_D k_B T \ln [J_0 / J_{SC}] \quad (1b)$$

where q is the electron charge, n_D is the ideality factor resulting from charge recombination due to traps in the donor layer, k_B is the Boltzmann constant, T is the temperature, k_{PPd} is the PP dissociation rate, $k_{rec,n}$ is the bimolecular recombination rate for trapped holes and free electrons, N_L is the band-edge density of states for the acceptor LUMO, H_D is the defect density of states on the donor side of the heterojunction, J_X is the exciton flux density arriving at the D–A junction, and a_0 is the spatial extent of PPs across the interface. Here, the saturation current density

is given by: $J_0 = qa_0 k_{PPd} k_{rec,n} N_L H_D / (k_{PPd} + k_{PPr})$, and the short circuit current density is related to the exciton current via: $J_{SC} = qJ_X k_{PPd} / (k_{PPd} + k_{PPr})$.

It is apparent from the foregoing that k_{PPr} directly affects both V_{OC} (due to an increase in J_0) and J_{SC} , and must be minimized to increase both of these key performance parameters. Other work has aimed to reduce k_{PPr} by adding steric hindrance to reduce orbital overlap at the D–A interface, but additional steric bulk can increase the resistivity and reduce the exciton diffusivity in the bulk.^{4,10,13} Here, we achieve the reduction in k_{PPr} using *only* morphological control over a bilayer structure achieved in a one-step annealing process.

Annealing is commonly used to modify film crystallinity and morphology.¹⁴ Annealing (whether by thermal or SV processes) promotes D–A phase separation and coarsening of bulk heterojunction morphology^{15–20} and aids in crystallization, thereby improving exciton diffusivity and charge mobility.^{19–23} In particular, SVA promotes molecular mass transport over large distances and can result in crystallites that are tens or even hundreds of micrometers in length.^{14,22} Annealing often decreases V_{OC} for a particular material pair,^{18,23–25} which has, in some cases, been attributed to changes in molecular orientation at the D–A interface that enhances intermolecular electronic coupling, thereby increasing k_{PPr} .¹⁰ Additionally, the spatial orientation of the donor at the D–A interface has been shown to affect V_{OC} by modifying ΔE_{HL} .²⁶ Finally, annealing is known to drive impurities to grain boundaries,²⁷ leading to an accumulation of defects at the D–A interface. These defects, whether originating from morphology or impurities, can increase both k_{PPr} and H_D , also reducing V_{OC} , according to eq 1.

Here we compare DPSQ/ C_{60} devices that are solvent vapor annealed in a saturated dichloromethane (DCM) vapor, either before or after the C_{60} deposition, to as-cast devices (see Methods). X-ray diffraction measurements (Figure 1a) on the as-cast DPSQ/ C_{60} layers lack DPSQ diffraction peaks, indicative of an amorphous film. In contrast, peaks due to C_{60} diffraction (solid arrows) show weak ordering in the acceptor layer. On the other hand, films annealed prior to the deposition of C_{60} (pre- C_{60}) exhibit a weak DPSQ diffraction peak (dashed arrow) at $2\theta = 5.9 \pm 0.1^\circ$ with a full-width at half-maximum (fwhm) of $0.4 \pm 0.1^\circ$. From these data, we calculate a d -spacing of $15.0 \pm 0.3 \text{ \AA}$ for DPSQ, which is not found in single crystals of DPSQ grown from solution.⁵ This, along with strengthened C_{60} peaks (at $2\theta = 10.8^\circ$, 17.7° , and 20.7°), indicates increased order in both layers. The improved C_{60} crystallinity suggests that the crystallized DPSQ acts as a structural template for the subsequent growth of C_{60} .²⁶ Templating arises from intimate molecular contact across the D–A interface. Finally, the post- C_{60} film shows no DPSQ diffraction peaks, yet the C_{60} peaks are stronger than for the as-cast film, indicating improved crystalline order in the C_{60} , but reduced order compared to the pre- C_{60} films.

The absorption spectrum of the as-cast (i.e., disordered) DPSQ consists of a single peak at a wavelength of $\lambda \approx 750 \text{ nm}$. For SVA films, the absorption is split into two peaks centered at $\lambda \approx 720 \text{ nm}$ and $\lambda \approx 785 \text{ nm}$ that are characteristic of aggregation, as shown in Figure 1b. The similarity of the aggregation splitting in the pre- C_{60} and post- C_{60} absorption spectra suggest that the DPSQ is, indeed, crystallizing in the post- C_{60} treatment, but with a significantly smaller crystallite size or orientational order that goes undetected by X-ray diffraction. This confirms that the extent of crystalline order in

the post- C_{60} film is between that of the as-cast and pre- C_{60} films.

Combining information from absorption and X-ray diffraction studies provides further information about the electronic structure at the interface. On crystallization, materials generally have a slightly reduced HOMO–LUMO energy gap due to electronic state delocalization across several molecules. Therefore, when crystallinity is extended to the D–A interface, ΔE_{HL} will likely decrease, and k_{ppr} increases compared to disordered interfaces where adjacent molecules are poorly electronically coupled.

Atomic force microscope (AFM) images show layer roughening during SVA (see Figure 2). When neat, 40 nm-

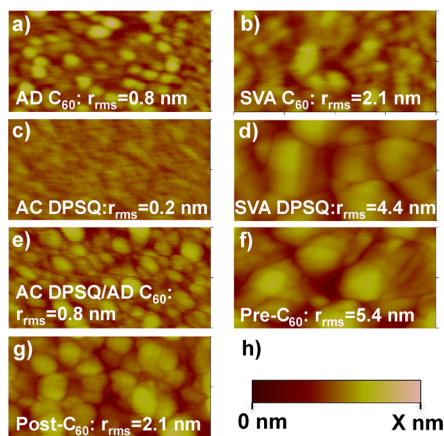


Figure 2. Film morphologies as determined by atomic force microscopy. Root-mean-square roughness (r_{rms}) and scale bar values (X) are given for: (a) as-deposited (AD) C_{60} , $r_{rms} = 0.8$ nm, $X = 10$ nm; (b) SVA C_{60} , $r_{rms} = 2.1$ nm, $X = 20$ nm; (c) as-cast (AC) DPSQ, $r_{rms} = 0.2$ nm, $X = 5$ nm; (d) SVA DPSQ, $r_{rms} = 4.4$ nm, $X = 50$ nm; (e) AC DPSQ with AD C_{60} , $r_{rms} = 0.8$ nm, $X = 20$ nm; (f) SVA DPSQ with AD C_{60} , $r_{rms} = 5.4$ nm, $X = 50$ nm (i.e., pre- C_{60}); (g) SVA after DPSQ and C_{60} depositions, $r_{rms} = 2.1$ nm, $X = 20$ nm (i.e., post- C_{60}); (h) Height scale bar. The images have fields of view of $1 \mu\text{m} \times 0.5 \mu\text{m}$.

thick layers of C_{60} deposited on MoO_3 (Figure 2a) are solvent vapor annealed (Figure 2b), the root-mean-square film roughness (r_{rms}) increases from $r_{rms} = 0.8 \pm 0.1$ nm to $r_{rms} = 2.1 \pm 0.2$ nm, while the roughness of a 16 ± 1 nm-thick DPSQ film (Figure 2c) increases 20-fold, from $r_{rms} = 0.2 \pm 0.1$ nm to $r_{rms} = 4.4 \pm 0.2$ nm (Figure 2d). This indicates that DPSQ molecules are more mobile along the film surface than C_{60} during SVA. When C_{60} is deposited on an as-cast DPSQ layer (Figure 2e), the roughness increases from $r_{rms} = 0.2 \pm 0.1$ nm to $r_{rms} = 0.8 \pm 0.1$ nm. In contrast, and when C_{60} is deposited on SV-annealed DPSQ (e.g., pre- C_{60} , Figure 2f), the roughness increases from $r_{rms} = 4.4 \pm 0.2$ nm to $r_{rms} = 5.4 \pm 0.3$ nm. A film of DPSQ capped with a layer of C_{60} was also annealed (i.e., post- C_{60} , Figure 2g), in which case the roughness increased from $r_{rms} = 0.8 \pm 0.1$ nm to only $r_{rms} = 2.1 \pm 0.2$ nm, which is equal to that of the annealed neat C_{60} layer.

These results demonstrate that capping the DPSQ with C_{60} prior to SVA significantly limits the long-range reorganization in the DPSQ layer beneath it, thereby maintaining the planarity of the D–A interface. This is similar to the effects of applying a metallic “stressor” overlayer, previously shown by Peumans et al.,¹⁹ to maintain organic surface planarity while allowing the internal film structure to change during thermal annealing.

The J – V characteristics for the devices fabricated using these various annealing sequences are shown in Figure 3, with J_{SC}

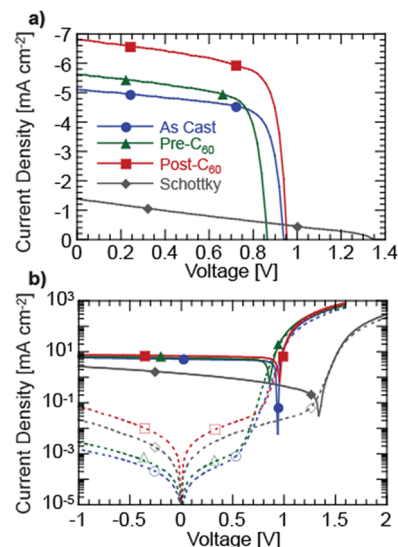


Figure 3. Performance of the DPSQ/ C_{60} devices. (a) Fourth-quadrant illuminated current density–voltage (J – V) characteristics of as-cast, pre- C_{60} , post- C_{60} , and MoO_3 – C_{60} Schottky devices. (b) $\ln(J)$ – V characteristics for illuminated (1 sun) and dark conditions (line colors and symbols correspond to those in Figure 3a). Illuminated conditions are indicated by solid lines and filled symbols, and dark conditions are shown by dotted lines and open symbols.

V_{OC} , FF, and η_p listed in Table 1. Compared to as-cast devices, the pre- C_{60} process results in a reduction in V_{OC} from 0.94 ± 0.01 V to 0.86 ± 0.01 V, leading to a concomitant decrease in power conversion efficiency from $\eta_p = 3.6 \pm 0.2\%$ to $3.4 \pm 0.2\%$. In contrast, the post- C_{60} process significantly improves device performance: that is, J_{SC} increases from 5.3 ± 0.3 $\text{mA}\cdot\text{cm}^{-2}$ for the as-cast structures, to 7.0 ± 0.4 $\text{mA}\cdot\text{cm}^{-2}$, leading to a corresponding improvement in efficiency from $\eta_p = 3.6 \pm 0.2\%$ to $4.8 \pm 0.3\%$ (see Figure 3 and Table 1). The differences in saturation current density, J_0 , and ideality factor, n , under dark conditions are apparent in Figure 3b, with their values listed in Table 1. As noted in eq 1, the value of J_0 is a function of the recombination rate, k_{ppr} , and directly affects V_{OC} .

The effects of SVA on J_{SC} can be further understood from the external quantum efficiency (EQE) measurements in Figure 4. The pre- C_{60} process increases EQE by $\sim 30\%$ in the spectral region associated with DPSQ (at $\lambda = 550$ – 820 nm). Analysis of the AFM data shows a 2% increase in surface area for SVA DPSQ compared to the as-cast surface, which is insufficient to result in the observed increase in EQE. In contrast, the EQE contribution from C_{60} is decreased by 10% compared to the as-cast device, even though the crystallinity of the C_{60} has increased due to SVA. Finally, post- C_{60} devices have an increased EQE across their entire spectrum, as shown in Figure 4. We attribute these increases in EQE on annealing to the improved crystalline morphology of the resulting films observed in Figure 1. Crystallinity results in an extended exciton diffusion length and hence a more efficient exciton transport to the donor–acceptor junction.³

The 32% increase in J_{SC} on post- C_{60} SVA should result in an increase in V_{OC} of 0.01 V, according to eq 1. The measured increase is 0.02 V, which is within the experimental error of

Table 1. Performance Parameters for the Excitonic DPSQ/C₆₀ Heterojunction Solar Cells

film process	J_{SC} (mA·cm ⁻²)	V_{OC} (V)	FF (%)	η_p (%)	J_0 (mA·cm ⁻²)	n	k_{ppr}/k_{ppd}
as-cast	5.3 ± 0.3	0.94 ± 0.01	73 ± 1	3.6 ± 0.2	(6.4 ± 1.7) × 10 ⁻¹²	1.37 ± 0.02	
pre-C ₆₀	5.6 ± 0.3	0.86 ± 0.01	70 ± 1	3.4 ± 0.2	(3.3 ± 0.9) × 10 ⁻¹¹	1.34 ± 0.02	0.26 ± 0.10
post-C ₆₀	7.0 ± 0.4	0.96 ± 0.01	71 ± 1	4.8 ± 0.3	(1.1 ± 0.3) × 10 ⁻¹²	1.29 ± 0.02	0.009 ± 0.006
Schottky	1.2 ± 0.1	1.34 ± 0.02	27 ± 2	0.4 ± 0.1	(3.3 ± 1.6) × 10 ⁻¹⁵	1.67 ± 0.05	

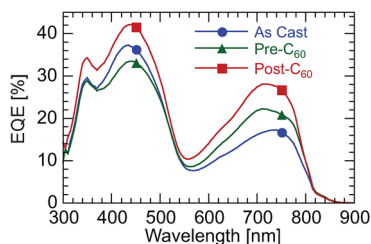


Figure 4. Optical response of the DPSQ/C₆₀ devices. External quantum efficiencies (EQE) of as-cast, pre-C₆₀, and post-C₆₀ devices are shown.

± 0.01 V. This is striking evidence that there is negligible change in the interface morphology with the post-C₆₀ SVA process that would otherwise introduce changes in the PP recombination rate, k_{ppr} . Rather, the improvement introduced by SVA following C₆₀ deposition is due to molecular reorganization in the bulk that improves exciton diffusivity and charge transport without altering the interface structure (including defects, order, and orientation). The reduction in EQE for pre-C₆₀ relative to the post-C₆₀ and as-cast devices suggests a partial quenching of excitons at the pre-C₆₀ D–A interface (i.e., k_{ppr} is increased), consistent with the reduction in V_{OC} and J_{SC} (c.f. eq 1).¹

Since $J_0 = H_D \cdot k_{ppr} / (k_{ppd} + k_{ppr})$,¹ the relationship between k_{ppd} and k_{ppr} for heterojunctions subjected to different annealing procedures can be calculated from the dark J – V characteristics in Figure 3b. We find that $k_{ppr}/k_{ppd} = \sim 0.01$ for the post-C₆₀ device and ~ 0.26 for the pre-C₆₀ device (see Table 1). The increase in k_{ppr}/k_{ppd} from post-C₆₀ to pre-C₆₀ is likely overestimated due to an increase in H_D and a possible decrease in J_X for the post-C₆₀ device, which have not been included in the analysis. Nevertheless, our results indicate that the change in EQE and J_0 results from a change in carrier recombination dynamics at the D–A interface due to morphological changes inferred from data in Figures 1 and 2.

To further understand the origin of the morphological and performance characteristics of the heterojunctions, X-ray photoemission spectra (XPS) were obtained for the as-cast and SVA DPSQ films. As shown in Figure 5a, there is an increase in the magnitude of peaks associated with ITO and MoO₃ after SVA, indicating that the MoO₃ buffer layer and the ITO anode are exposed through voids formed on recrystallization. The MoO₃–C₆₀ interface forms a Schottky junction with a $V_{OC} = 1.34$ V (see Figure 3 and Table 1)²⁸ that reduces leakage through shunt paths formed within the voids that would otherwise short the D–A heterojunction.

Finally, ultraviolet photoemission spectroscopy (UPS) was used to measure the ionization energy, which in the case of semiconductors with a low concentration of free carriers is congruent with the HOMO energy. From this measurement we, therefore, infer changes in ΔE_{HL} that occur on annealing. The HOMO energies of the DPSQ are -5.1 ± 0.1 eV and -5.2 ± 0.1 eV (relative to vacuum), with work functions of $0.53 \pm$

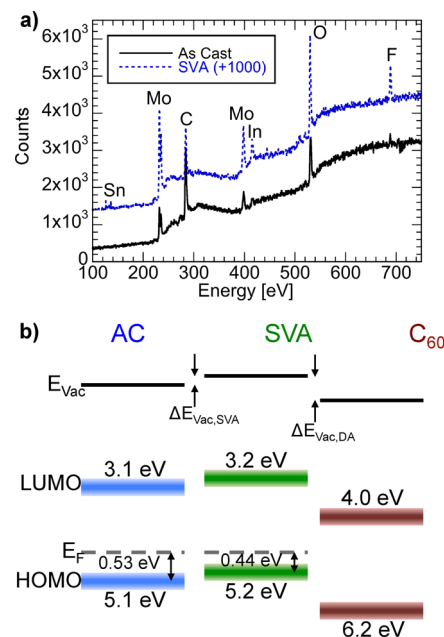


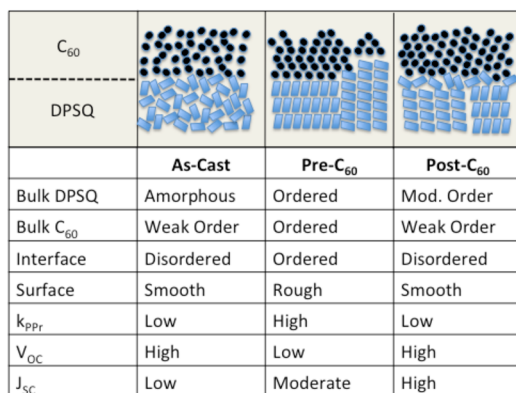
Figure 5. Photoemission spectra of DPSQ. (a) X-ray photoemission spectra of as-cast (AC) and solvent vapor annealed (SVA, offset 1000 counts for clarity) samples. With SVA, an increase in magnitude of responses from In, Sn, Mo, and oxygen is observed. The fluorine impurity peak is occasionally detected for both as-cast and SVA samples (see Methods). (b) Energy level diagrams for AC and SVA DPSQ and C₆₀. The HOMO energy levels and the position of the Fermi energy (E_F) for DPSQ were measured using ultraviolet photoelectron spectroscopy, while the LUMO levels are estimated from ref 5, and the C₆₀ energies are taken from refs 33 and 34. $\Delta E_{vac,SVA}$ is the change in interface dipole energy due to SVA, and $\Delta E_{vac,DA}$ is the interface dipole (value unknown) present at the D–A heterojunction shown for a SVA-processed DPSQ/C₆₀ junction. Also, ΔE_{HL} is shown for the SVA DPSQ–C₆₀ donor–acceptor pair.

0.10 eV and 0.44 ± 0.10 eV (defined relative to the HOMO, but are physically measured relative to the vacuum level) for the as-cast and SVA films, respectively, as shown in Figure 5b. The change in HOMO energy on SVA suggests an increased ΔE_{HL} , which should lead to an increase in V_{OC} of similar magnitude. However, in this case, V_{OC} is reduced. The difference in work function indicates that the interface dipole at the DPSQ surface is also affected by the SVA process. This interface dipole, although within the measurement error, could lead to a reduction in $\Delta E_{HL} = 0.1$ eV, consistent with the 0.08 V reduction in V_{OC} observed for the respective devices.

Note that, in blends of 1-NPSQ and DPASQ²⁵ the efficiencies are improved for post-C₆₀ SVA, although at the expense of a small reduction in V_{OC} . This suggests that the stability of D–A interface morphology after SVA is materials system dependent. Additionally, the efficiency of SQ:PC₇₀BM blended cells is improved for relatively short SVA times (~ 10 min), but as the annealing time and hence the crystallinity of the SQ is increased further, a decrease in both J_{SC} and V_{OC} is

observed,¹⁸ suggesting that extensive crystallization results in an increase in k_{ppr} .

In conclusion, we find that SVA of DPSQ in the presence of an overlayer of C_{60} preserves the disorder at the D–A interface achieved on deposition, while introducing order into the bulk, whereas junctions annealed pre- C_{60} have increased order at the interface. This independent control of bulk and interface morphologies is a powerful means for controlling the PP recombination kinetics at excitonic heterojunctions while creating advantageous transport properties characteristic of an ordered film bulk. A summary of our findings for all heterojunction processing conditions is provided in Figure 6.



The figure consists of a schematic diagram at the top and a table below it. The schematic shows three cross-sectional views of a heterojunction. The top layer is labeled C_{60} and the bottom layer is labeled DPSQ. The first view is labeled 'As-Cast', the second 'Pre- C_{60} ', and the third 'Post- C_{60} '. The schematic shows the morphology of the layers: As-Cast shows a disordered interface and amorphous bulk; Pre- C_{60} shows an ordered interface and ordered bulk; Post- C_{60} shows a disordered interface and mod. order bulk.

	As-Cast	Pre- C_{60}	Post- C_{60}
Bulk DPSQ	Amorphous	Ordered	Mod. Order
Bulk C_{60}	Weak Order	Ordered	Weak Order
Interface	Disordered	Ordered	Disordered
Surface	Smooth	Rough	Smooth
k_{ppr}	Low	High	Low
V_{OC}	High	Low	High
J_{SC}	Low	Moderate	High

Figure 6. Qualitative summary of the structural and performance outcomes induced by the processing conditions discussed in text. Here, k_{ppr} is the polaron pair recombination rate, V_{OC} is the open circuit voltage, and J_{SC} is the short circuit current.

The results are understood in terms of the theory of ideal excitonic heterojunctions of Giebink et al., which provides a roadmap for optimizing the performance of OPV cells. The model DPSQ/ C_{60} OPV cell undergoes a 25% increase in power conversion efficiency to $\eta_p = 4.8 \pm 0.3\%$ compared to an analogous as-cast heterojunction through independent interface and bulk morphological control via SVA.

Methods. The OPV device structure is glass/indium tin oxide (ITO, 70 nm)/ MoO_3 (15 nm)/DPSQ (10 nm)/ C_{60} (40 nm)/PTCBI (5 nm)/Ag (100 nm). ITO-coated (15 Ω /sq) glass substrates were detergent and solvent cleaned, CO_2 snow cleaned,^{29,30} and exposed to ultraviolet light and ozone for 10 min prior to loading into a vacuum thermal evaporation (VTE) chamber (base pressure of $<1 \times 10^{-7}$ Torr). All devices used DPSQ recrystallized from a 1:1 volume ratio of dichloromethane (DCM) and methanol, as described previously.⁵ Based on data from mass and ultraviolet/visible spectroscopy as well as high-performance liquid chromatography (HPLC) measurements, impurities in the DPSQ can be identified as the corresponding regioisomeric DPSQs where one or both carbon atoms of the four-membered squarate rings attach to N-phenyl ring instead of N-(3,5-dihydroxyphenyl) rings of the triarylamine moiety. Material was purified by repetitive crystallization from hot chlorobenzene or toluene until $>99.8\%$ purity was achieved, as determined by HPLC. Devices made with the low and high purity DPSQ showed similar efficiency values and comparable behavior on SVA.

The substrates were first coated with a 15 nm thick layer of thermally evaporated MoO_3 (Alfa Aesar, 99.9995% purity). The DPSQ was dissolved in chloroform at 1–4 mg/mL, filtered through a 20 nm diameter pore anodic alumina filter using a

stainless steel filter housing, and spun-cast at a rate of 1000 rpm giving a thickness of 8–30 nm. The C_{60} (40 nm thick, MER- or Alfa Aesar-sublimed grade with one additional vacuum thermal gradient purification), buffer layers consisting of 3,4,9,10-perylenetetracarboxylic bisbenzimidazole (PTCBI, 5 nm-thick, Sensient Technologies Corp. sublimed grade),³¹ and the Ag cathodes (100 nm thick, through an array of 1 mm diameter holes in a shadow mask, Alfa Aesar, 99.999% purity) were subsequently deposited using VTE. Film thicknesses were measured using variable-angle spectroscopic ellipsometry.

At various points during fabrication, SVA was performed in sealed 500 mL vials containing an excess of DCM for 10 min. The annealing time was chosen to optimize both efficiency improvements and yield. Significant morphological and electrical changes were only observed for solvent exposures >7 min. Annealing >10 min produced incremental improvements in device performance, although the C_{60} layer roughened substantially, leading to device shorts and reduced yield.

The EQE was measured using a lock-in amplifier and a fiber-coupled monochromated Xe arc-discharge lamp (fwhm ≈ 15 nm). The optical power was calibrated using a NIST-traceable Si photodetector. Photovoltaic performance was tested with a semiconductor parameter analyzer using simulated air mass 1.5 global (AM1.5G) illumination, where illumination intensity was measured with an NREL-traceable KG-5 filtered Si reference cell. Spectral mismatch corrections (ranging from $M = 0.96$ to 0.99) were calculated using lamp spectral data obtained with a spectrometer calibrated using a NIST-traceable light source.³² Performance parameters are reported for the best repeatable efficiencies for the given device architecture. Errors for V_{OC} and FF arise from variations between devices, and the error in J_{SC} is primarily from uncertainty in measuring the intensity and spectrum of the lamp, which also dominates the error in η_p . Ideality factors (n) and saturation current density (J_0) were extracted from the dark J – V curves using the equation for a single-diode with a series resistance¹ using a least-squares fit.

Film characterization by tapping-mode atomic force microscopy was obtained for 16 ± 1 nm thick DPSQ and 40 ± 1 nm thick C_{60} films deposited on MoO_3 -coated Si substrates. X-ray diffraction measurements were obtained using Cu- $K\alpha$ radiation and a θ – 2θ double-crystal configuration for ~ 30 nm thick DPSQ and 40 nm thick C_{60} layers deposited on MoO_3 -coated (001) silicon. Errors are quoted for variations between measurements on multiple samples. Absorptivity measurements were made on structures with 30 nm thick DPSQ and 40 nm thick C_{60} films deposited on MoO_3 -coated quartz substrates. Photoemission spectroscopy measurements were obtained using 16 nm thick DPSQ films on MoO_3 -coated ITO substrates in ultrahigh vacuum with a Thermo VG Scientific Clam 4MCD analyzer. The He-I emission line was used for UPS and Al- $K\alpha$ radiation for XPS. Beginning with the MoO_3 deposition, all device processing, current–voltage, quantum efficiency, XPS, and UPS measurements were performed without exposure to ambient, with all transfers and processing done in ultrahigh purity nitrogen-filled glove boxes. Fluorine impurities are occasionally observed via XPS for both purities (see above) and for as-cast and SVA samples. No correlation between device performance parameters (i.e., V_{OC} , J_{SC} , or FF) and the presence of fluorine has been observed.

AUTHOR INFORMATION

Notes

The authors declare the following competing financial interest(s): Two of the authors (M.E.T. and S.R.F.) have an equity interest in one of the sponsors of this work (GPEC).

ACKNOWLEDGMENTS

The authors thank B. E. Lassiter for useful discussions. Financial support was provided by the Air Force Office of Scientific Research (C.K.R., UPS, and XPS), and The Center for Solar and Thermal Energy Conversion at the University of Michigan (Award No. DE-SC00000957; J.D.Z., experiment and analysis, X.X., device fabrication), the NSF SOLAR program (S.R.F., analysis; M.E.T., V.V.D., and S.W., synthesis), and Global Photonic Energy Corp.

REFERENCES

- Giebink, N. C.; Wiederrecht, G. P.; Wasielewski, M. R.; Forrest, S. R. *Phys. Rev. B* **2010**, *82*, 155305.
- Giebink, N. C.; Lassiter, B. E.; Wiederrecht, G. P.; Wasielewski, M. R.; Forrest, S. R. *Phys. Rev. B* **2010**, *82*, 155306.
- Lunt, R. R.; Benziger, J. B.; Forrest, S. R. *Adv. Mater.* **2010**, *22*, 1233.
- Schlenker, C. W.; Barlier, V. S.; Chin, S. W.; Whited, M. T.; McAnally, R. E.; Forrest, S. R.; Thompson, M. E. *Chem. Mater.* **2011**, *23*, 4132–4140.
- Wang, S.; Hall, L.; Diev, V. V.; Haiges, R.; Wei, G.; Xiao, X.; Djurovich, P. I.; Forrest, S. R.; Thompson, M. E. *Chem. Mater.* **2011**, *23*, 4789–4798.
- Wei, G.; Xiao, X.; Wang, S.; Sun, K.; Bergemann, K. J.; Thompson, M. E.; Forrest, S. R. *ACS Nano* **2011**, *6*, 972–978.
- Forrest, S. R.; Kaplan, M. L.; Schmidt, P. H. *J. Appl. Phys.* **1984**, *56*, 543–551.
- Warta, W.; Stehle, R.; Karl, N. *Appl. Phys. A: Mater. Sci. Process.* **1985**, *36*, 163–170.
- Peumans, P.; Yakimov, A.; Forrest, S. R. *J. Appl. Phys.* **2003**, *93*, 3693–3723.
- Perez, M. D.; Borek, C.; Forrest, S. R.; Thompson, M. E. *J. Am. Chem. Soc.* **2009**, *131*, 9281–9286.
- Potsavage, J. W. J.; Yoo, S.; Kippelen, B. *Appl. Phys. Lett.* **2008**, *93*, 193308–3.
- Marsh, R. A.; McNeill, C. R.; Abrusci, A.; Campbell, A. R.; Friend, R. H. *Nano Lett.* **2008**, *8*, 1393–1398.
- Erwin, P.; Thompson, M. E. *Appl. Phys. Lett.* **2011**, *98*, 223305.
- De Luca, G.; Pisula, W.; Credgington, D.; Treossi, E.; Fenwick, O.; Lazzerini, G. M.; Dabirian, R.; Orgiu, E.; Liscio, A.; Palermo, V.; Müllen, K.; Cacialli, F.; Samorì, P. *Adv. Funct. Mater.* **2011**, *21*, 1279–1295.
- Li, G.; Shrotriya, V.; Huang, J.; Yao, Y.; Moriarty, T.; Emery, K.; Yang, Y. *Nat. Mater.* **2005**, *4*, 864–868.
- Chen, F. C.; Ko, C. J.; Wu, J. L.; Chen, W. C. *Sol. Energy Mater. Sol. Cells* **2010**, *94*, 2426–2430.
- Wei, G. D.; Wang, S. Y.; Renshaw, K.; Thompson, M. E.; Forrest, S. R. *ACS Nano* **2010**, *4*, 1927–1934.
- Wei, G. D.; Wang, S. Y.; Sun, K.; Thompson, M. E.; Forrest, S. R. *Adv. Energy Mater.* **2011**, *1*, 184–187.
- Peumans, P.; Uchida, S.; Forrest, S. R. *Nature* **2003**, *425*, 158–162.
- Dittmer, J. J.; Lazzaroni, R.; Leclère, P.; Moretti, P.; Granström, M.; Petritsch, K.; Marseglia, E. A.; Friend, R. H.; Brédas, J. L.; Rost, H.; Holmes, A. B. *Sol. Energy Mater. Sol. Cells* **2000**, *61*, 53–61.
- Wei, G. D.; Lunt, R. R.; Sun, K.; Wang, S. Y.; Thompson, M. E.; Forrest, S. R. *Nano Lett.* **2010**, *10*, 3555–3559.
- Conboy, J. C.; Olson, E. J. C.; Adams, D. M.; Kerimo, J.; Zaban, A.; Gregg, B. A.; Barbara, P. F. *J. Phys. Chem. B* **1998**, *102*, 4516–4525.
- Placencia, D.; Wang, W. N.; Shallcross, R. C.; Nebesny, K. W.; Brumbach, M.; Armstrong, N. R. *Adv. Funct. Mater.* **2009**, *19*, 1913–1921.
- Gregg, B. A. *J. Phys. Chem.* **1996**, *100*, 852–859.
- Xiao, X.; Wei, G.; Wang, S.; Zimmerman, J. D.; Renshaw, C. K.; Thompson, M. E.; Forrest, S. R. *Adv. Mater.* **2012**, *24*, 1956–1960.
- Lassiter, B. E.; Lunt, R. R.; Renshaw, C. K.; Forrest, S. R. *Opt. Express* **2010**, *18*, A444–A450.
- Kazmerski, L. L.; Ireland, P. J.; Cizek, T. F. *Appl. Phys. Lett.* **1980**, *36*, 323–325.
- Zhang, M.; Irfan, Ding, H.; Gao, Y.; Tang, C. W. *Appl. Phys. Lett.* **2010**, *96*, 183301.
- Wang, N.; Zimmerman, J. D.; Tong, X.; Xiao, X.; Yu, J.; Forrest, S. R. **2012**, submitted.
- Sherman, R.; Grob, J.; Whitlock, W. J. *Vac. Sci. Technol. B* **1991**, *9*, 1970–1977.
- Lassiter, B. E.; Wei, G.; Wang, S.; Zimmerman, J. D.; Diev, V. V.; Thompson, M. E.; Forrest, S. R. *Appl. Phys. Lett.* **2011**, *98*, 243307.
- Seaman, C. H. *Sol. Energy* **1982**, *29*, 291–298.
- Sato, N.; Saito, Y.; Shinohara, H. *Chem. Phys.* **1992**, *162*, 433–438.
- Shirley, E. L.; Louie, S. G. *Phys. Rev. Lett.* **1993**, *71*, 133–136.